as a dSph is not yet conclusive, but the similarities between the dwarf and the rest of the Galactic dSphs are compelling.

The close proximity to the Galactic Centre, the morphological appearance and the radial velocity of 140 km s^{-1} indicate that this system is currently undergoing strong tidal disruption before being integrated into the Milky Way. The tidal limit for a bound system of similar dynamical mass to Fornax, at a distance of 16 kpc from the Galactic Centre, is ~0.5 kpc. As Sagittarius extends over at least 3 kpc, almost an order of magnitude larger than the tidal limit, it provides us with a snapshot of an early phase of the tidal destruction of a satellite galaxy. □

Received 5 April; accepted 7 June 1994.

1. Burstein, D. & Heiles, C. *Astr. J.* **87,** 1165–1189 (1982).
2. Tonry, J. & Davies, M. *Astr. J.* **84,** 1511–1525 (1979).
3. Lewis, J. & Freeman, K. *Astr. J.* **97,** 139–162 (1989).
4. Kibblewhite, E., Bridgeland, M., Bunclark, P. & Irwin, M. in *Proc. Astronomical Microdensitometry Conf.* 277–288 (NASA-CP-2317, 1984).
5. Gardiner, L. & Hatzidimitriou, D. *Mon. Not. R. astr. Soc.* **257,** 195–224 (1992).
6. Feast, M. in *The Magellanic Clouds* (eds Haynes, R. & Milne, D.) 1–5 (Int. Astr. Un. Symp. No. 148, Kluwer Academic, Dordrecht, 1991).
7. Sagar, R., Hawkins, M. & Cannon, R. *Mon. Not. R. astr. Soc.* **242,** 167–176 (1990).
8. Caldwell, N., Armandroff, T., Seitzer, P. & Da Costa, G. *Astr. J.* **103,** 840–850 (1992).
9. Irwin, M. & Hatzidimitriou, D. in *ASP Conf. Ser.* Vol. 48 (eds Smith, G. & Brodie, J.) 322–325 (Astr. Soc. Pacific, San Francisco, 1993).
10. Demers, S., Irwin, M. & Kunkel, W. *Astr. J.* (in the press).

ACKNOWLEDGEMENTS. The Sagittarius dwarf galaxy was found using a combination of UK Schmidt Telescope sky survey plates, the APM automatic plate measuring facility and the Anglo Australian Telescope multifibre spectrograph, AUTOFIB. We thank the staff of these institutions for the facilities and service that they provide.

Preparation and structure of crystals of the metallofullerene $Sc_2@C_{84}$

R. Beyers*, C-H. Kiang*†, R. D. Johnson*, J. R. Salem*, M. S. de Vries*, C. S. Yannoni*, D. S. Bethune*, H. C. Dorn‡, P. Burbank‡, K. Harich‡ & S. Stevenson‡

* IBM Research Division, Almaden Research Center, 650 Harry Road, San Jose, California 95120–6099, USA
† Materials and Molecular Simulation Center, Beckman Institute, California Institute of Technology, Pasadena, California 91125, USA
‡ Department of Chemistry, Virginia Polytechnic Institute and State University, Blacksburg, Virginia 24061, USA

IT was first proposed in 1985[1] that fullerenes can confine atoms in their interior because of their closed-cage structure. Attempts to verify this conjecture following the mass production of fullerenes[2,3] have yielded metallofullerenes in bulk, and there is now good evidence that these compounds are endohedral[4]—that is, that the metal atoms are inside. But direct confirmation in the form of structural data has been lacking, in part because of the difficulty of separating different metallofullerenes and obtaining pure crystals. Here we report the preparation of pure crystalline $Sc_2@C_{84}$ and analyses of its structure by electron diffraction and high-resolution transmission electron microscopy. At room temperature the $Sc_2@C_{84}$ molecules pack in a hexagonal-close-packed structure with a ratio of lattice constants $c/a = 1.63$, the value expected for ideal-sphere packing. The molecular spacing of 11.2 Å is the same as that found earlier in crystalline C_{84} (refs 5, 6). The match between our microscopic images and simulations is markedly better for endohedral models than for those in which the metal atoms reside in the lattice outside the C_{84} cages. We believe that this combination of observations points inevitably to the conclusion that the metal atoms are inside the fullerenes.

Interest in metallofullerene compounds is motivated by the possibility that appropriate internal dopants can be used to tune the physical and chemical properties of the molecules, giving rise to a family of materials with potential applications as catalysts, nonlinear optical or ferroelectric materials, transport agents for refractory or reactive species, photosensitizers or electronic materials. Metallofullerenes containing Y, Sc or lanthanide atoms form readily, and have been characterized by a variety of methods[4], but detailed characterization and structural studies have been impeded by the difficulty of preparing pure samples. Methods for purifying these species using multiple stages of high-performance liquid chromatography (HPLC) have been reported recently[7–10], and initial characterization work, including ultraviolet-visible spectroscopy[7,8], infrared spectroscopy[8] and scanning tunnelling microscopy[11] has been done.

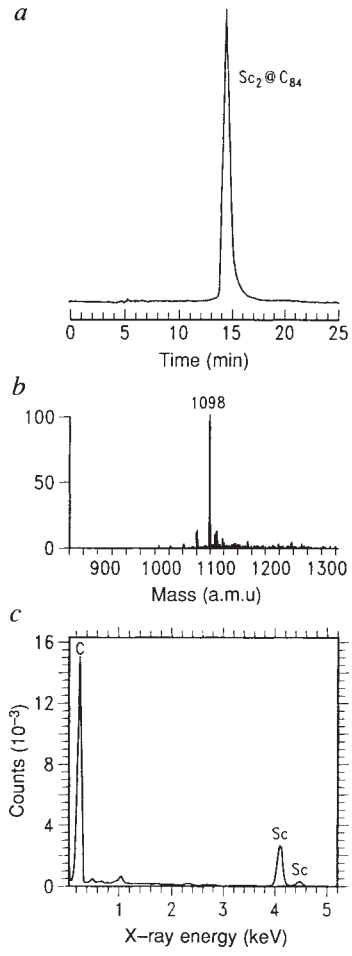

FIG. 1 *a*, HPLC trace for the purified $Sc_2@C_{84}$ sample obtained using ultraviolet detection at 340 nm; *b*, Negative-ion chemical-ionization mass spectrum of the $Sc_2@C_{84}$ fraction indicating ~80% purity, with ~10% each of $Sc_2@C_{82}$ and a species tentatively identified as $(Sc_2C)@C_{84}$; *c*, Energy dispersive X-ray spectrum of a $Sc_2@C_{84}$ crystal.

We prepared metallofullerenes by arc-vaporizing 6-mm diameter cored-carbon rods, packed with a mixture of Sc or Sc_2O_3 and graphite powders, in 200 torr of helium with ~100 A direct current. Metal loadings of 1–3 at% (with respect to total carbon) were used. The soot was promptly extracted with CS_2. Purification was accomplished by methods similar to those described in the literature[7,8], but with the HPLC system fully automated to allow unattended operation[9], and equipped with both ultraviolet and on-line electron paramagnetic resonance (EPR) detection to allow isolation of fractions containing monometal and trimetal metallofullerenes[10]. A toluene/decalin (80/20) mixture with relatively high solubility for fullerenes and metallofullerenes was used as the eluent, allowing relatively large quantities of material (≥10 mg) to be injected onto the columns. Coarse separation of metallofullerenes from empty fullerenes was achieved using polystyrene columns. A second HPLC stage using a Buckyclutcher (Regis Chemical Co., Morton Grove, Illinois) column separated the different metallofullerenes. Further details will be published elsewhere[9,10]. The dominant scandium metallofullerenes were discandium species with cages of 74, 76,

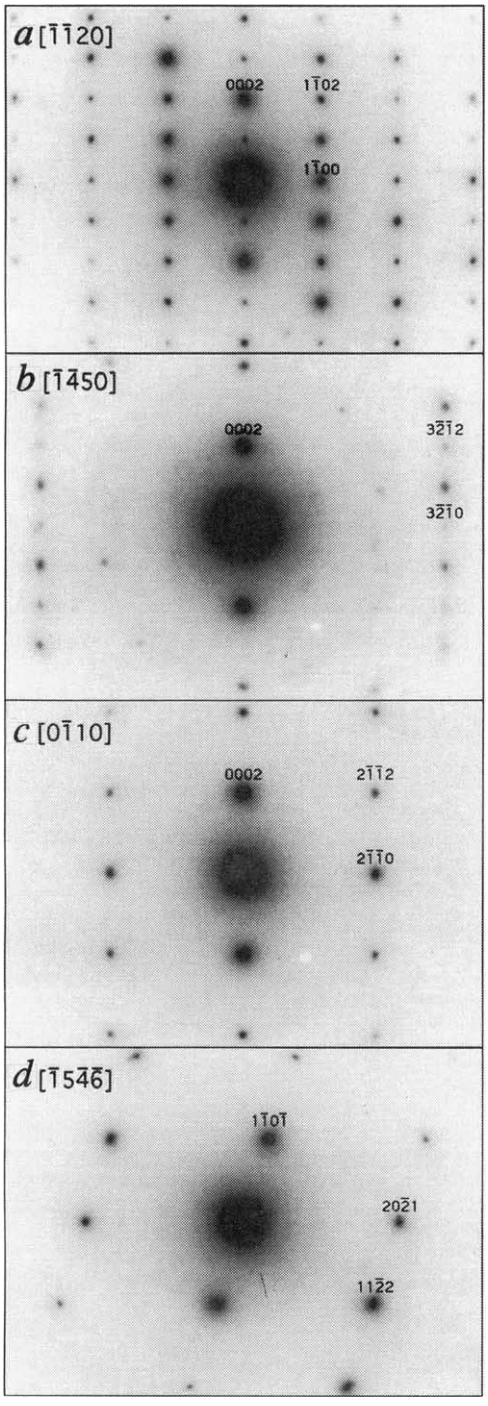

FIG. 2 Electron diffraction zone-axis patterns of $Sc_2@C_{84}$, taken along the [1̄1̄20] (*a*), [1̄450] (*b*), [01̄10] (*c*) and [1̄54̄6] (*d*) directions.

or even numbers of carbons between 80–104, with $Sc_2@C_{84}$ the most abundant[9,10]. Figure 1 shows analytical data for the purified $Sc_2@C_{84}$. An HPLC trace for the final $Sc_2@C_{84}$ sample is shown in Fig. 1*a*, and the corresponding negative-ion chemical-ionization mass spectrum is shown in Fig. 1*b*. $Sc_2@C_{84}$ constitutes ~80% of this sample, with $Sc_2@C_{82}$ accounting for an additional 10%. A peak near 1,110 atomic mass units (a.m.u.) (also ~10%), may be due to $(Sc_2C)@C_{84}$, $Sc_2@C_{84}O$ and/or ScO_2C_{86}. A number of peaks possibly corresponding to odd-carbon metallofullerenes were found in other HPLC fractions. A second $Sc_2@C_{84}$ isomer (confirmed by mass spectrometry) was completely resolved by HPLC at a retention time shorter than that for the major $Sc_2@C_{84}$ isomer studied here. This second species was also obtained as a pure sample.

Crystals were grown by dissolving the $Sc_2@C_{84}$ in CS_2 and allowing the solvent to evaporate slowly. These crystals were suspended in ethanol and placed on a holey carbon grid for examination by transmission electron microscopy (TEM), performed in a Topcon 002B instrument operating at either 100 or 200 kV. The lower voltage was used for high-resolution imaging because electron-beam damage occurred quite rapidly when a 200 kV beam was focused onto a $Sc_2@C_{84}$ crystal. Crystals with dimensions ranging from 1 to 20 μm were observed. Elemental analysis of the crystals by energy dispersive X-ray spectroscopy (EDS) showed principally carbon and scandium (Fig. 1*c*). Sulphur (presumably from CS_2) could also be detected in some crystals, but was absent from others ($S/Sc < 0.05$).

Electron diffraction patterns from sulphur-free crystals are shown in Fig. 2. These patterns indicate that $Sc_2@C_{84}$ crystallizes in a hexagonal-close-packed (h.c.p.) structure, with lattice parameters $a = 11.2 \pm 0.2$ Å and $c = 18.3 \pm 0.2$ Å, giving a c/a ratio of 1.63. The observed reflections are consistent with the hexagonal space group $P6_3/mmc$. In Fig. 2*a*, the (0001) and (0003) reflections arise because of double diffraction; these reflections disappeared when the crystal was tilted slightly off the [1̄1̄20] zone axis. No streaks were observed in the diffraction patterns, indicating that no stacking faults were present that would locally change the h.c.p. structure to a face-centred cubic (f.c.c.) structure.

High-resolution TEM images looking along the orthogonal [0001] and [1̄1̄20] directions are shown in Figs 3 and 4, respectively. In an h.c.p. structure, the close-packed planes have an ABAB . . . stacking sequence along the *c* axis, whereas the close-packed planes in an f.c.c. structure have an ABCABC . . . stacking sequence. The ABAB . . . stacking expected for an h.c.p. structure is evident in Fig. 4, and in Fig. 3 the prominent bright dots correspond to the aligned columns of unoccupied C sites. These images also confirm directly the absence of stacking faults and the lattice parameters measured by electron diffraction.

Detailed consideration of high-resolution TEM images such as those in Figs 3 and 4, and the electron diffraction data in Fig. 2, leads us to conclude that the scandium atoms in $Sc_2@C_{84}$ are inside the carbon cage. In thin ($\leqslant 100$ Å) fullerene crystals near Scherzer defocus, there is a one-to-one correspondence between the projected crystal potential and the high-resolution image[12]. For example, columns of empty C_{60} and C_{70} are imaged as dark rings around a bright central spot[13].

The TEM image in Fig. 3*a* looks down the *c* axis of a $Sc_2@C_{84}$ crystal. The black features correspond to the overlapping projections of the carbon cages of molecules centred at the A and B sites, whereas the grey features in Fig. 3*a–c* are centred on these molecules. Comparing these grey features with the corresponding (but brighter) areas in the simulated image for empty C_{84} (Fig. 3*d*) shows that there is additional projected charge density within columns of $Sc_2@C_{84}$ molecules for this viewing direction.

The TEM image in Fig. 4*a* was obtained with the crystal oriented so that the $Sc_2@C_{84}$ molecules are stacked in columns normal to the image plane. The columns of molecules appear as dark circles, indicating that the additional charge density associated with the Sc atoms is located within these columns. This result is supported by comparing the image with simulated TEM images for empty (Fig. 4*d*) and Sc-containing (Fig. 4*c*) C_{84} molecules arranged in an h.c.p. structure. The simulation for the empty cages shows the expected bright central spots, which are absent from the image for the metal-filled species. Taken together, these projected images looking along two perpendicular crystal directions provide strong evidence that the metal atoms are within the C_{84} cages. This location is further supported by the diffraction data, which shows that the nearest-neighbour separation for $Sc_2@C_{84}$ is the same as that found previously for C_{84} (11.2 Å)[5,6].

NMR studies[14–17] and theoretical calculations[18–22] indicate

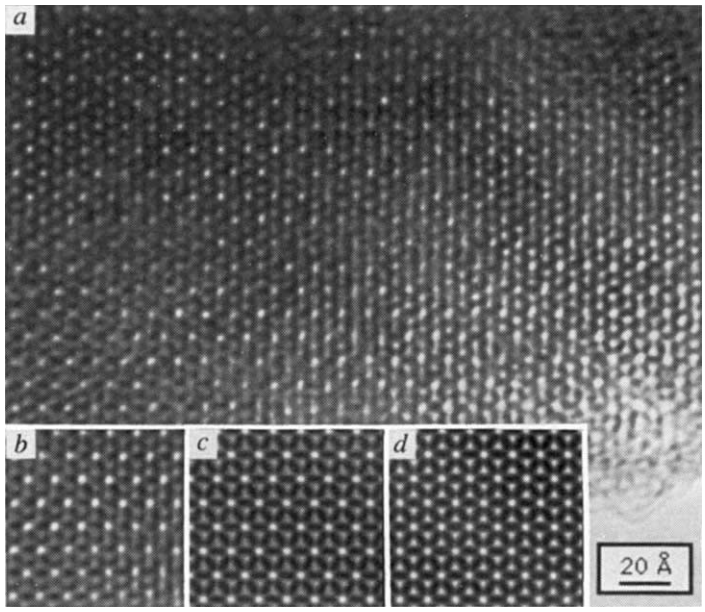

FIG. 3 *a*, High-resolution TEM image of a $Sc_2@C_{84}$ crystal, taken along the [0001] direction. Inset *b* is a Fourier-filtered image that brings out the periodicities present in the original image. Insets *c* and *d* are simulated images of 67 Å thick $Sc_2@C_{84}$ and C_{84} crystals, respectively, at −500 Å defocus. In *c* and *d*, three different orientations of the molecules are superimposed to simulate the orientational disorder present in the crystals.

that empty C_{84} consists of a 2:1 mixture of $D_2(22)$ and $D_{2d}(23)$ isomers (in the notation of Manolopolous and Fowler[23]). The presence of analogous isomers of $Sc_2@C_{84}$ would result in disorder within the crystals. Moreover, the fact that $Sc_2@C_{84}$ crystals have the c/a ratio expected for hexagonal close-packing of perfect spheres ($c/a=\sqrt{8/3}\approx 1.63$), even though the isomers of the $Sc_2@C_{84}$ molecule are not perfectly spherical, indicates that there is orientational disorder (either static or dynamic) of the molecules within the crystals at room temperature. This conclusion is supported by comparison of experimental and simulated high-resolution images. The match between these images is improved if several different orientations of the $Sc_2@C_{84}$ molecule are superimposed (Figs 3 and 4), rather than having unique, fixed positions for the Sc and C within the unit cell.

The matching intermolecular spacing in $Sc_2@C_{84}$ and C_{84} indicates that possible charge transfer to the cage in $Sc_2@C_{84}$ does not significantly increase its van der Waals radius. The C_{84} cage diameter (extrapolated from 7.1 Å for C_{60} by assuming equal surface densities of carbon atoms) is estimated to be 8.4 Å. Thus the distance between the carbon cages in crystals of both C_{84} and $Sc_2@C_{84}$ is ~2.8 Å. This can be compared with the cage spacing of 2.87 Å for C_{60} crystals derived from the ball diameter[24] and lattice parameter[25] found in earlier studies. The conclusion that the van der Waals radii of $Sc_2@C_{84}$ and C_{84} are the same contrasts with the conclusion drawn from STM studies[11] that $Sc@C_{74}$ and $Sc_2@C_{74}$ have larger diameters than would be expected from the diameter of the corresponding empty fullerene cage (~7.9 Å), possibly due to charge transfer from the metal atoms to the cage. □

Received 2 December 1993; accepted 14 June 1994.

1. Kroto, H. W., Heath, J. R., O'Brien, S. C., Curl, R. F. & Smalley, R. E. *Nature* **318,** 162–163 (1985).

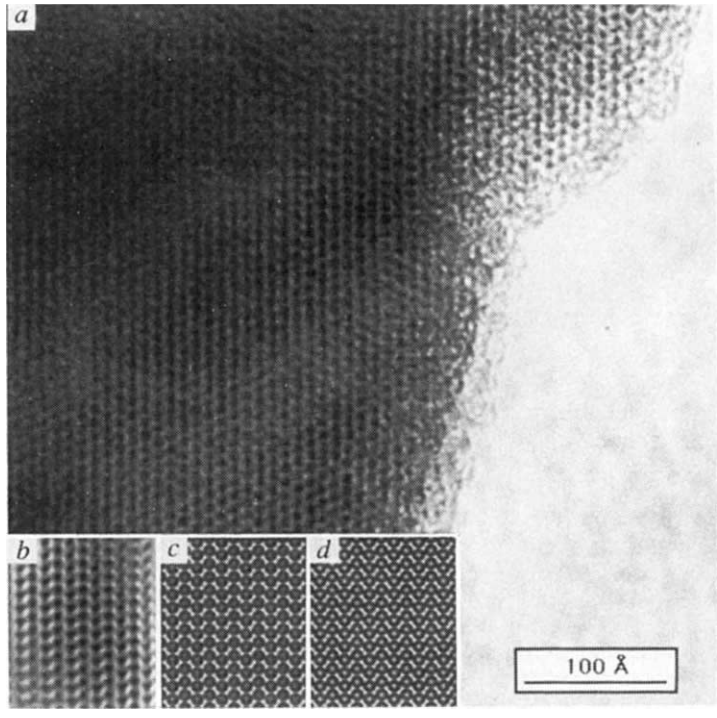

FIG. 4 *a*, High-resolution TEM image of a $Sc_2@C_{84}$ crystal, taken along the [1120] direction. Inset *b* is a Fourier-filtered image that brings out the periodicities present in the original image. Insets *c* and *d* are simulated images of 22 Å thick $Sc_2@C_{84}$ and C_{84} crystals, respectively, at −500 Å defocus. In *c* and *d*, orientational disorder is simulated by the same method employed in Fig. 3.

2. Krätschmer, W., Fostiropoulos, K. & Huffman, D. R. *Chem. Phys. Lett.* **170,** 167–170 (1990).
3. Krätschmer, W., Lamb, L. D., Fostiropoulos, K. & Huffman, D. R. *Nature* **347,** 354–358 (1990).
4. Bethune, D. S., Johnson, R. D., Salem, J. R., de Vries, M. S. & Yannoni, C. S. *Nature* **366,** 123–128 (1993).
5. Saito, Y., Yoshikawa, T., Fujimoto, N. & Shinohara, H. *Phys. Rev.* B**48,** 9182–9185 (1993).
6. Armbruster, J. F. *et al. Phys. Rev.* B (submitted).
7. Shinohara, H. *et al. J. phys. Chem.* **97,** 4259–4261 (1993).
8. Kikuchi, K. *et al. Chem. Phys. Lett.* **216,** 67–91 (1993).
9. Dorn, H. C. *et al. Analyt. Chem.* (in the press).
10. Stevenson, S. *et al. Analyt. Chem.* (in the press).
11. Wang, X. *et al. Jap. J. appl. Phys.* **32,** L866–L868 (1993).
12. Van Tendeloo, G. & Amelinckx, S. *Adv. Mater.* **5,** 620–629 (1993).
13. Muto, S. *et al. Phil. Mag.* B**67,** 443–463 (1993).
14. Kikuchi, K. *et al. Chem. Lett.* **16,** 1607–1610 (1991).
15. Diederich, F. & Whetten, R. L. *Accts. Chem. Res.* **25,** 119–126 (1992).
16. Kikuchi, K. *Nature* **357,** 142–145 (1992).
17. Manolopolous, D. E., Fowler, P. W., Taylor, R., Kroto, H. W. & Walton, D. *J. chem. Soc., Faraday Trans.* **88,** 3117–3118 (1992).
18. Zhang, X. W. & Ho, D. S. *Phys. Rev. Lett.* **69,** 69–72 (1992).
19. Raghavachari, K. *Chem. Phys. Lett.* **190,** 397–400 (1992).
20. Wang, B. L. & Ho, D. S. *J. chem. Phys.* **96,** 7183–7185 (1992).
21. Bakoies, D. *et al. Chem. Phys. Lett.* **200,** 411–417 (1992).
22. Schneider, U., Richard, S., Kappes, M. M. & Ahlrichs, R. *Chem. Phys. Lett.* **210,** 165–169 (1993).
23. Manolopolous, D. E. & Fowler, P. W. *J. chem. Phys.* **96,** 7603–7614 (1992).
24. Yannoni, C., Bernier, P., Bethune, D., Meijer, G. & Salem, J. *J. Am. chem. Soc.* **113,** 3190–3192 (1991).
25. Fleming, R. *et al.* in *Proc. Mater. Res. Soc.* Vol. 206 (eds Averback, R. S., Berhole, J. & Nelson, D. L.) 691–696 (Materials Research Soc., Pittsburgh, 1991).

ACKNOWLEDGEMENTS. We thank D. Dorn and L. Jackson for technical assistance, and acknowledge financial support from the Virginia Center for Innovative Technology. C.H.K. acknowledges support from the US NSF and the Materials and Molecular Simulation Center (supported by DOE-AICD, Allied-Signal, BP America, Asahi Chemical, Asahi Glass, Chevron, BF Goodrich and Xerox).

Biological magnetic resonance imaging using laser-polarized ^{129}Xe

M. S. Albert*, G. D. Cates†, B. Driehuys†, W. Happer†, B. Saam†, C. S. Springer Jr* & A. Wishnia*‡

* Department of Chemistry, State University of New York, Stony Brook, New York 11794-3400, USA
† Department of Physics, Princeton University, Princeton, New Jersey 08544, USA

As currently implemented, magnetic resonance imaging (MRI) relies on the protons of water molecules in tissue to provide the NMR signal. Protons are, however, notoriously difficult to image in some biological environments of interest, notably the lungs[1] and lipid bilayer membranes such as those in the brain[2]. Here we show that ^{129}Xe gas can be used for high-resolution MRI when the nuclear-spin polarization of the atoms is increased by laser optical pumping and spin exchange[3–6]. This process produces hyperpolarized ^{129}Xe, in which the magnetization is enhanced by a factor of about 10^5. By introducing hyperpolarized ^{129}Xe into mouse lungs we have obtained images of the lung gas space with a speed and a resolution better than those available from proton MRI[1,7] or emission tomography[8,9]. As xenon (a safe general anaesthetic) is rapidly and safely transferred from the lungs to blood and thence to other tissues[8,9], where it is concentrated in lipid[10–15] and protein[13,15–18] components, images of the circulatory system, the brain and other vital organs can also be obtained. Because the magnetic behaviour of ^{129}Xe is very sensitive to its environment, and is different from that of ^1H_2O, MRI using hyperpolarized ^{129}Xe should involve distinct and sensitive mechanisms for tissue contrast.

The magnetic resonance signal strength of a given nuclear species depends on its total magnetization in the chosen sample volume element; that is, on the product of the species concentration, the excess spin density per nucleus (polarization), and the volume of the element. In the largest available magnetic fields, thermal-equilibrium polarizations reach $\sim 10^{-5}$, which is adequate for ^1H_2O imaging. Other proton species, and all other nuclear species, have concentrations too small to be of use in conventional high-speed, high-resolution MRI. Xenon gas at 1 atm, for example, has a molar concentration only 0.04% that of tissue ^1H_2O. However, the polarization of ^{129}Xe and other spin 1/2 noble gases can be enormously enhanced through spin-exchange with an optically pumped alkali metal vapour[3–5]. In our case, a dilute vapour of rubidium (~1 p.p.m. of the Xe pressure) is kept spin-polarized by the absorption of 1–2 W of circularly polarized 795-nm Rb D_1-resonance light from a Ti:sapphire laser. Gas-phase collisions between the ^{129}Xe and the polarized Rb atoms result in the transfer of angular momentum from the Rb valence electron to the ^{129}Xe nucleus. The ^{129}Xe gas is laser-polarized to at least 25% in 5–20 min (depending on conditions), enhancing its NMR signal to $\sim 10^5$ times the thermal equilibrium value. The gas is then delivered for imaging.

Figure 1*a–c* shows the evolution in time (0–10 s) of the distribution of hyperpolarized ^{129}Xe entering the lungs of a mouse lung–heart preparation. In Fig. 1*a* the xenon has just begun to enter the lungs. In Fig. 1*b* the lungs are so inflated that they press against the interior of the 10-mm diameter glass tube in which they are contained. Finally, in Fig. 1*c* the lungs have started to deflate and the two lobes are clearly visible. The bright spot toward the centre is a cross-section of the trachea through which the xenon was introduced. All three ^{129}Xe images are dark in the region between the lung lobes where the heart is located. Comparison with a standard ^1H_2O image (Fig. 1*d*), in which the heart is prominent and the lungs invisible, illustrates one aspect of the complementary nature of proton- and ^{129}Xe-MRI. All ^{129}Xe images in Fig. 1 were obtained in 600 ms at an average lung Xe concentration of ~20 mM (1.2×10^{19} atoms cm^{-3}), which is tiny compared to the 80–100 M proton concentrations typical of ^1H_2O imaging; yet the signal intensities, spatial resolution (0.14–0.28 mm^3), and data acquisition rates all exceed those obtained in standard clinical ^1H_2O-MRI. Moreover, the magnetization densities are so large that several images can be generated in rapid succession, allowing for real-time tracking of physiological processes.

The large and long-lived ^{129}Xe magnetization densities achieved in the lung provide a basis for imaging beyond the lung itself—MRI of ^{129}Xe transported from the lung to various tissues is feasible. To assess the MRI parameters for ^{129}Xe in lipid environments we imaged a tube of octanol, a standard cell-membrane model, containing dissolved (205 mM) thermally-polarized xenon. The images were of lower resolution (20 mm^3) and required 7 min to obtain but clearly demonstrate the feasibility of using ^{129}Xe to image tissue. With hyperpolarized ^{129}Xe, high-resolution images comparable to those of Fig. 1 could be obtained in a single rapid imaging scan, even for the lower concentrations expected in tissue. In the brain, for example, a xenon concentration of ~10 mM is expected for a subject breathing 50% xenon[15].

Imaging with a hyperpolarized species depends on the transport of sufficient surviving magnetization to tissues of interest. The polarization decays with the longitudinal relaxation time T_1, which must be long in the lungs and blood. We have measured $T_1 \sim 30$ s for gaseous ^{129}Xe in the excised mouse lungs. Adjusting for the O_2-relaxivity[19] in a normally breathing subject we project values of 12–15 s in the lung. We also obtained a T_1 value of ~40 s for ^{129}Xe dissolved in partly deoxygenated rat blood. We estimate T_1 for ^{129}Xe in fully-oxygenated cell membranes to be >15 s (refs 15, 20, 21). This estimate must be compared to the time it takes for xenon to reach various tissues. Inhaled xenon reaches equilibrium with the entire blood volume in one blood circuit, (~1 s in a mouse, and ~15 s in a human[9,22,23]). As transport and relaxation times are of the same order of magnitude, one can expect significant accumulation of highly polarized ^{129}Xe in all tissues.

The importance of this technique hinges on the radically

‡ To whom correspondence should be addressed.